

Evidence for environmental effects in the $z = 4.3$ protocluster core SPT2349–56

CHAYCE HUGHES,¹ RYLEY HILL,¹ SCOTT C. CHAPMAN,^{2,3,1} MANUEL ARAVENA,⁴ MELANIE ARCHIPLEY,^{5,6}
VERONICA J. DIKE,⁷ ANTHONY GONZALEZ,⁸ THOMAS R. GREVE,^{9,10} GAYATHRI GURURAJAN,^{11,12} CHRIS HAYWARD,¹³
KEDAR PHADKE,⁷ CASSIE REUTER,¹⁴ JUSTIN SPILKER,¹⁵ NIKOLAUS SULZENAUER,¹⁶ JOAQUIN D. VIEIRA,^{7,17,18}
DAVID VIZGAN,⁷ GEORGE WANG,¹ AXEL WEISS,¹⁶ AND DAZHI ZHOU¹

¹University of British Columbia, 6225 Agricultural Road, Vancouver, V6T 1Z1, Canada

²Dalhousie University, 5071 W Saanich Rd, Halifax, B3H 4R2, Canada

³NRC–Herzberg Astronomy and Astrophysics, 5071 W Saanich Rd, Victoria, V9E 2E7, Canada

⁴Instituto de Estudios Astrofísicos, Facultad de Ingeniería y Ciencias, Universidad Diego Portales, Av. Ejército 441, Santiago, 8320000, Chile

⁵Kavli Institute for Cosmological Physics, University of Chicago, 5640 South Ellis Avenue, Chicago, IL 60637, USA

⁶Department of Astronomy and Astrophysics, University of Chicago, 5640 South Ellis Avenue, Chicago, IL 60637, USA

⁷Department of Astronomy, University of Illinois, 1002 West Green Street, Urbana, IL 61801, USA

⁸Department of Astronomy, University of Florida, 211 Bryant Space Science Center, Gainesville, FL 32611-2055, USA

⁹Cosmic Dawn Center (DAWN), Technical University of Denmark, DTU Space, Elektrovej 327, 2800 Kgs Lyngby, Denmark

¹⁰Department of Physics and Astronomy, University College London, Gower Street, London, WC1E 6BT, UK

¹¹Scuola Internazionale Superiore Studi Avanzati (SISSA), Physics Area, Via Bonomea 265, 34136 Trieste, Italy

¹²IFPU-Institute for Fundamental Physics of the Universe, Via Beirut 2, 34014 Trieste, Italy

¹³Center for Computational Astrophysics, Flatiron Institute, 162 Fifth Avenue, New York, NY 10010, USA

¹⁴Department of Physics, University of California, 366 Physics North MC 7300, Berkeley, CA, 94720-7300, USA

¹⁵Department of Physics and Astronomy and George P. and Cynthia Woods Mitchell Institute for Fundamental Physics and Astronomy, Texas A&M University, 4242 TAMU, College Station, TX 77843-4242, USA

¹⁶Max-Planck-Institut für Radioastronomie, Auf dem Hügel 69, Bonn, D-53121, Germany

¹⁷Center for AstroPhysical Surveys, National Center for Supercomputing Applications, 1205 West Clark Street, Urbana, IL 61801, USA

¹⁸Department of Physics, University of Illinois, 1110 West Green St., Urbana, IL 61801, USA

ABSTRACT

We present ALMA observations of the [CII] 492 and 806 GHz fine-structure lines in 25 dusty star-forming galaxies (DSFGs) at $z = 4.3$ in the core of the SPT2349–56 protocluster. The protocluster galaxies exhibit a median $L'_{[\text{CII}](2-1)}/L'_{[\text{CII}](1-0)}$ ratio of 0.94 with an interquartile range of 0.81–1.24. These ratios are markedly different to those observed in DSFGs in the field (across a comparable redshift and 850 μm flux density range), where the median is 0.55 with an interquartile range of 0.50–0.76, and we show that this difference is driven by an excess of [CII](2–1) in the protocluster galaxies for a given 850 μm flux density. Assuming local thermal equilibrium, we estimate gas excitation temperatures of $T_{\text{ex}} = 59.1^{+8.1}_{-6.8}$ K for our protocluster sample and $T_{\text{ex}} = 33.9^{+2.4}_{-2.2}$ K for the field sample. Our main interpretation of this result is that the protocluster galaxies have had their cold gas driven to their cores via close-by interactions within the dense environment, leading to an overall increase in the average gas density and excitation temperature, and an elevated [CII](2–1) luminosity-to-far-infrared luminosity ratio.

Keywords: Galaxy environments(2029) — Protoclusters(1297) — High-redshift galaxies(734)

1. INTRODUCTION

In the local Universe, galaxies residing within galaxy clusters are significantly different from their field counterparts (e.g., Ellis et al. 1997; Andreon 2003; Muzzin et al. 2012): cluster galaxies are predominantly red ellipticals that stopped forming stars long ago, while field galaxies are predominantly blue spirals with much

higher star-formation rates (SFRs). At high redshift ($z \gtrsim 1.5$), when most galaxy clusters are not yet virialized (a regime in which we call these objects protoclusters), quiescent galaxies are much less common within overdense environments (e.g. Scoville et al. 2013). Indeed, some observations suggest that protoclusters are actually in an elevated state of star-formation compared

to the field (e.g., Overzier 2016; Chiang et al. 2017; Popescu et al. 2023), likely driven by mergers and interactions (e.g., Lotz et al. 2013; Hine et al. 2016; Andrews et al. 2024). However, the impacts that these processes imprint on protocluster galaxies are not well understood.

The difficulty in directly probing environmental effects on protocluster galaxies stems from the fact that at high redshift, the contrast against the field is typically not large, and subtle differences are often impacted by degeneracies and small sample sizes – these include differences in stellar ages (e.g., Steidel et al. 2005; Rettura et al. 2010; Lee-Brown et al. 2017; Webb et al. 2020), metallicities (e.g., Valentino et al. 2015; Namiki et al. 2019; Pérez-Martínez et al. 2024), and resolved distributions of star formation and stellar mass (e.g., Vulcani et al. 2018; Cramer et al. 2024), but there is no clear consensus on the importance (or existence, in some cases) of these differences.

The protocluster SPT2349–56 was discovered as a bright point source in the South Pole Telescope (SPT) 2500 deg² millimetre-wavelength survey (Everett et al. 2020), and it was later resolved into a collection of > 30 dusty star-forming galaxies (DSFGs) at $z = 4.3$ (Miller et al. 2018; Hill et al. 2020; Rotermund et al. 2021; Apostolovski et al. 2024). This system therefore presents an opportunity to directly observe how environmental effects arising from cluster formation are imprinted on cluster galaxies. By combining several continuum observations from the Atacama Large Millimeter/submillimeter Array (ALMA), *Spitzer*, *Gemini*, and the *Hubble Space Telescope* (*HST*), it appears that the protocluster galaxies in SPT2349–56 are consistent with the galaxy main sequence (i.e. field galaxies) around redshift 4 (Rotermund et al. 2021; Hill et al. 2022). On the other hand, detections of the CO(4–3) transition (which is approximately proportional to gas mass) provided tentative evidence that the gas depletion timescales (defined as the ratio of gas mass to SFR) in the SPT2349–56 protocluster galaxies are shorter than for field galaxies (Hill et al. 2022), but more evidence is needed.

While observations of the total CO spectral line energy distribution (SLED) would provide more accurate constraints on the total gas mass, lower J lines (especially $J = 1$) typically lack the spatial resolution to resolve many of the sources in the crowded SPT2349–56 protocluster. However, Zhou et al. (2025) recently showed that observations of the CO(4–3) line towards the SPT2349–56 protocluster core from the Atacama Compact Array (ACA) recovered a 75% excess in integrated line strength compared to ALMA observations of the individual galaxies. The low angular resolution of

the ACA observations effectively blended all of the protocluster galaxies into a single unresolved sources, meaning that a significant amount of gas (traced by CO(4–3)) must exist as extended emission outside of the individual protocluster galaxies, effectively resolved out by the high angular resolution of ALMA; similar conclusions have been discussed with regard to other protoclusters such as the Distant Red Core (DRC) at $z = 4.0$ (Oteo et al. 2018; Ivison et al. 2020).

In this paper we use the neutral carbon atom ([C I]) to further probe environmental effects on the properties of the SPT2349–56 galaxies. The two neutral atomic carbon fine structure lines ([C I](1–0), $\nu_{\text{rest}} = 492.2$ GHz, and [C I](2–1), $\nu_{\text{rest}} = 809.3$ GHz) fall within ALMA’s Bands 3 and 4 at $z = 4.3$, respectively. Owing to the simple three-level quantum structure of atomic carbon, the ratio of line luminosities can be used to probe the excitation temperature of the [C I] gas (e.g., Weiß et al. 2003; Walter et al. 2011; Bothwell et al. 2017; Gururajan et al. 2023). This offers a simple approach to probe the internal state of protocluster galaxies and field galaxies. Moreover, [C I] (as an alternative to CO) has been proposed as a tracer of molecular gas (e.g., Weiß et al. 2003; Papadopoulos & Greve 2004; Dunne et al. 2021), allowing for an independent assessment of the gas content in the SPT2349–56 sample. Throughout this paper we assume the Λ CDM cosmology from Planck Collaboration VI (2020) (1 arcsec = 6.9 kpc at $z = 4.3$).

2. DATA

2.1. ALMA observations and data reduction

The [C I](1–0) transition redshifts to 92.9 GHz at $z = 4.3$, which can be observed by ALMA in Band 3. This transition was observed by the ALMA program 2017.1.00273.S (PI S. Chapman), taken as a two-pointing mosaic targeting all of the known core-component and northern-component protocluster galaxies reported in Hill et al. (2020). The [C I](2–1) transition redshifts to ALMA’s Band 4 at 152.7 GHz; the core galaxies were observed by ALMA programs 2018.1.00018.S (PI S. Chapman) and 2021.1.01313.S (PI R. Canning), while the northern galaxies were only observed by the latter program. The array configuration used in both Band 4 observing programs were similar and the spectral coverages were configured to be nearly identical. The [C I](2–1) line is partially blended (depending on the linewidth) with the CO(7–6) line ($\nu_{\text{rest}} = 806.7$ GHz, redshifted to 152.2 GHz at $z = 4.3$), which we also observe for all of our targets.

The data were calibrated with the standard observatory-provided `ScriptForPI` scripts using the versions of CASA (McMullin et al. 2007) appropriate to

the ALMA cycle. For the Band 4 observations of the core galaxies, we combined the fully-calibrated visibilities from both observing programs into a single measurement set. Data cubes were made using the `CASA` function `tclean` with Briggs weighting and a robust parameter of 0.5, auto-masking, and cleaning down to a threshold of 0.1 mJy (roughly 2σ per channel for all of the cubes). The average synthesized beamsize for the Band 3 data cube sideband containing the line emission of interest was $1.4 \text{ arcsec} \times 1.0 \text{ arcsec}$ and $0.34 \text{ arcsec} \times 0.29 \text{ arcsec}$ for the Band 4 data cube.

2.2. Line measurements

Essentially all of the sources are unresolved in the Band 3 data, so a peak-pixel spectrum approach was used to extract spectra from the data cube. Using the redshifts and line widths taken from the best-fit [CII] line profiles from Hill et al. (2020), we averaged over the channels within 2σ of the expected position of the [CI](1–0) line and searched for the brightest pixels near the galaxy positions given in Hill et al. (2020). We then extracted the spectrum at the brightest pixel position. In the Band 4 data the sources are typically resolved, so we designed circular apertures for each source. The center and radius of each aperture was set to enclose the 3σ contour of each source in the channel-averaged map, again using the positions of known galaxies from Hill et al. (2020) as a prior. We also tested using aperture photometry on the Band 3 data, finding the aperture measurements of the [CI](1–0) line did not change the signal compared to the peak pixel measurements while significantly increasing the uncertainties.

The per-channel noise in the peak pixel spectra was estimated by first masking all the sources with circular masks of the same shape and position as the Band 4 apertures. At each channel, we used sigma clipping with a 3.5σ limit to estimate the standard deviation of the background noise pixels. To estimate the per-channel noise in the aperture spectra, we first masked all the sources with circular masks of the same shape and position as the apertures. For each source we then drew 1300 apertures at random positions and then calculated the standard deviation of the 1300 random aperture flux densities. The peak pixel Band 3 and aperture Band 4 spectra of a representative subset of the target sources are shown in Fig. 1, with the continuum subtracted after fitting the line profiles (as described in detail below).

We deblended the CO(7–6) and [CI](2–1) lines in Band 4 using the method described in Chapman et al. (2024). Briefly, the best-fit [CII] line profiles from Hill et al. (2020) (where the fit was either a single or double Gaussian) were used as templates, redshifted to the expected

frequencies of the CO(7–6) and [CI](2–1) lines. For most sources, we fit the [CII] template to the data using three free parameters, namely the CO(7–6) amplitude, the [CI](2–1) amplitude, and the continuum level. Sources C3, C5, and N1 required the relative height of the two Gaussians composing their line profiles to be another free parameter. When measuring the line strength of the [CI](2–1) line we then subtract the fit to the CO(7–6) line, and vice versa. For completeness we followed the same approach to fit profiles to the [CI](1–0) lines, with only two free parameters describing the line height and continuum level. For the brighter sources, we confirmed that the [CII] profiles agreed with the measured CO and CI line profiles (see Fig. 1).

The line strengths were measured by integrating the channels over the region defined by the [CII] line profile: If the [CII] line profile consists of one Gaussian, then the integration region used was $\pm 1.6\sigma$ about the mean. If the [CII] line profile consists of two Gaussians, then the integration region is between $\mu_{\text{left}} - 1.6\sigma_{\text{left}}$ and $\mu_{\text{right}} + 1.6\sigma_{\text{right}}$, where μ and σ are the means and standard deviations of the ‘left’ and ‘right’ Gaussians, respectively. We then scaled the line strengths and errors by the ratio of the total area under the Gaussian to the expected flux inside the integration range, to account for faint flux density missing from the wings of the Gaussian line profiles. For a single Gaussian line profile, this ratio is 1.12. For a double Gaussian line profile, this ratio was calculated for each source (values range between 1.06 and 1.12). We also computed the spatial line emission cutouts for each line, by averaging the data cubes over the line emission channels described above after subtracting the continuum using the `CASA` task `imcontsub` using the remaining channels. We applied the same procedure to the CII data cubes, and in Appendix B we compare the results; we find that the expected [CI](1–0) and [CI](2–1) signals in our spectra spatially coincide with the [CII] emission.

Lastly, the integrated line strengths were converted to luminosities using the redshifts taken from the [CII] line centers in Hill et al. (2020). In Table 1 we provide our results for the [CI](1–0), [CI](2–1), and CO(7–6) line strengths, as well as 2 mm continuum flux densities from Band 4 (Band 3 continuum flux densities are already published in Hill et al. 2020). Where the signal is detected at $> 2\sigma$ we provide the value and the uncertainty, otherwise we provide 3σ upper limits.

3. RESULTS

Table 1. Summary of the observed line strength measurements and the observed flux density at $2000\,\mu\text{m}$, S_{2000} . The uncertainties are 1σ . Measurements below 2σ are shown as 3σ upper bounds.

ID	$L_{[\text{Cl}](1-0)}$ ($10^7 L_\odot$)	$L_{[\text{Cl}](2-1)}$ ($10^7 L_\odot$)	$L_{\text{CO}(7-6)}$ ($10^7 L_\odot$)	$F_{[\text{Cl}](1-0)}$ (Jy km s^{-1})	$F_{[\text{Cl}](2-1)}$ (Jy km s^{-1})	$F_{\text{CO}(7-6)}$ (Jy km s^{-1})	S_{2000} (mJy)
Core							
C1	3.86 ± 0.41	27.7 ± 2.4	34.7 ± 2.3	0.250 ± 0.026	1.089 ± 0.094	1.371 ± 0.089	1.091 ± 0.034
C2	0.63 ± 0.28	3.4 ± 1.2	7.8 ± 1.0	0.041 ± 0.018	0.132 ± 0.047	0.307 ± 0.041	0.302 ± 0.024
C3	4.01 ± 0.33	17.7 ± 1.1	23.7 ± 1.0	0.259 ± 0.021	0.698 ± 0.045	0.937 ± 0.040	0.899 ± 0.019
C4	3.01 ± 0.39	12.0 ± 1.8	8.9 ± 1.7	0.195 ± 0.025	0.471 ± 0.071	0.351 ± 0.066	0.840 ± 0.029
C5	2.56 ± 0.39	9.0 ± 1.9	7.0 ± 1.7	0.165 ± 0.025	0.355 ± 0.073	0.276 ± 0.067	0.626 ± 0.029
C6	2.12 ± 0.25	11.56 ± 0.63	19.49 ± 0.67	0.137 ± 0.016	0.455 ± 0.025	0.769 ± 0.026	0.624 ± 0.016
C7	1.18 ± 0.23	4.00 ± 0.89	5.67 ± 0.86	0.076 ± 0.015	0.157 ± 0.035	0.224 ± 0.034	<0.086
C8	1.03 ± 0.30	9.8 ± 1.3	12.0 ± 1.3	0.067 ± 0.020	0.387 ± 0.053	0.472 ± 0.051	0.560 ± 0.027
C9	1.31 ± 0.31	3.64 ± 0.89	9.42 ± 0.87	0.085 ± 0.020	0.143 ± 0.035	0.372 ± 0.034	0.097 ± 0.018
C10	0.68 ± 0.32	7.55 ± 0.89	10.90 ± 0.87	0.044 ± 0.021	0.297 ± 0.035	0.430 ± 0.034	0.135 ± 0.017
C11	<0.801	<3.135	3.76 ± 0.71	<0.052	<0.123	0.148 ± 0.028	0.054 ± 0.016
C12	<0.878	<0.417	<0.513	<0.057	<0.016	<0.020	<0.027
C13	0.42 ± 0.15	3.91 ± 0.91	6.06 ± 0.90	0.027 ± 0.010	0.154 ± 0.036	0.239 ± 0.036	0.381 ± 0.016
C14	<0.879	<1.695	<2.860	<0.057	<0.067	<0.113	0.043 ± 0.016
C15	1.10 ± 0.26	6.1 ± 1.7	4.4 ± 1.5	0.071 ± 0.017	0.239 ± 0.068	0.173 ± 0.059	0.158 ± 0.035
C16	0.62 ± 0.21	<1.245	<1.141	0.040 ± 0.014	<0.049	<0.045	<0.027
C17	<0.564	<1.616	<1.421	<0.036	<0.064	<0.056	<0.041
C18	<0.852	<3.549	<2.091	<0.055	<0.140	<0.083	<0.069
C19	0.79 ± 0.28	<4.522	<4.995	0.051 ± 0.018	<0.178	<0.197	0.098 ± 0.037
C20	<0.734	<1.360	<1.503	<0.048	<0.053	<0.059	0.098 ± 0.013
C21	0.43 ± 0.14	<1.145	<1.140	0.028 ± 0.009	<0.045	<0.045	0.046 ± 0.013
C22	0.138 ± 0.065	<0.806	<1.052	0.009 ± 0.004	<0.032	<0.042	<0.055
C23	<0.713	<1.039	<1.039	<0.046	<0.041	<0.041	<0.039
North							
N1	6.68 ± 0.37	25.4 ± 2.6	59.7 ± 2.6	0.432 ± 0.024	0.998 ± 0.101	2.356 ± 0.101	1.616 ± 0.043
N2	3.12 ± 0.45	23.0 ± 4.6	13.9 ± 4.6	0.202 ± 0.029	0.905 ± 0.183	0.547 ± 0.182	0.988 ± 0.078

To compare our measured line strengths with samples of field DSFGs at similar redshifts as SPT2349–56 we use S_{850} , the flux density at $850\,\mu\text{m}$, from Hill et al. (2020). S_{850} is model-independent, unlike quantities such as the far-infrared luminosity (L_{FIR}), and for $z \gtrsim 2$ is roughly independent of redshift. We note that while current dust continuum measurements of the protocluster galaxies in SPT2349–56 do not reach the peak of the SED at wavelengths around $500\,\mu\text{m}$, constraints on the average dust temperature of the protocluster population have been estimated to be about 40 K (Hill et al. 2020; Rotermund et al. 2021), although the uncertainties are still large. Additionally, high- J CO lines (such as $J=7$) have been suggested as tracers of L_{FIR} (Bayet et al. 2009; Liu et al. 2015), however the uncertainties in these scaling relations are comparable to the existing uncertainties in the dust temperatures.

In Fig. 2 we therefore plot our measured line luminosities as a function of S_{850} in three different ways: the top panel shows the ratio $L_{[\text{Cl}](2-1)} / L_{[\text{Cl}](1-0)}$, the ratio of the [Cl] line luminosities, while the bottom-left and bottom-right panels show $L_{[\text{Cl}](1-0)}$ and $L_{[\text{Cl}](2-1)}$, respectively. In the line ratio plot we also show the axis converted to $L'_{[\text{Cl}](2-1)} / L'_{[\text{Cl}](1-0)}$ (i.e. in units of $\text{K km s}^{-1} \text{pc}^2$), which are simply the original units multiplied by a factor of $(\nu_{[\text{Cl}](1-0)} / \nu_{[\text{Cl}](2-1)})^3$. In all panels we show these quantities as a function of S_{850} . In this plot we limit detections to $> 3.5\sigma$ and otherwise show 3σ upper/lower limits (depending on the quantity being plotted).

Our primary field comparison sample comes from Gururajan et al. (2023), which targeted [Cl](1–0) and [Cl](2–1) in a sample of 30 strongly-lensed sources se-

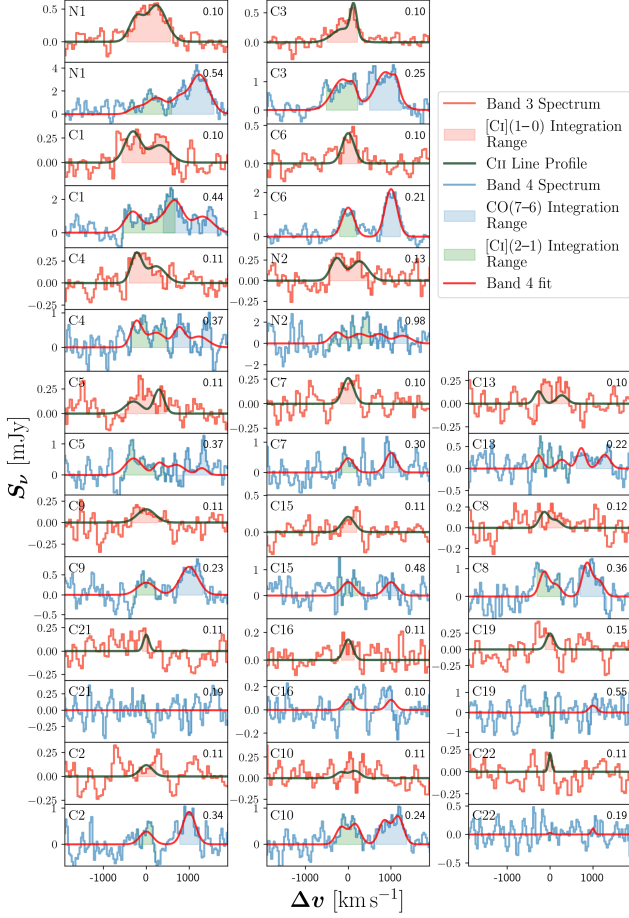


Figure 1. Continuum-subtracted Band 3 and 4 spectra for all sources with a $> 2\sigma$ peak pixel [CII](1–0) or aperture [CII](2–1) measurement. The average per-channel noise in mJy over the displayed channels is listed in the top-right of each panel, and the name of each galaxy in Hill et al. (2020) is listed in the top-left. All spectra are unbinned. The fits to the Band 3 and 4 spectra are shown in green and red, respectively. The scaled [CII] line profiles are overlaid on top of the Band 3 spectra. The shaded regions represent the integration ranges, although we note that we subtract the blended Band 4 lines before performing the integration. The sources are ordered by [CII](1–0) signal-to-noise ratio.

lected from the SPT sample (Reuter et al. 2020). The Gururajan et al. (2023) sample includes a single blended measurement of SPT2349–56, which we discard. Additionally, Gururajan et al. (2023) discard SPT0452–52 due to an ambiguous redshift at the time, leaving a sample of 28 DSFGs, 17 of which have good lens models (Spilker et al. 2016). CO(7–6) and CO(4–3) line luminosity measurements for this sample are also available (Gururajan, priv. comm.). [CII](2–1) and CO(7–6) deblending was done in a comparable way, and we checked that our deblending algorithm (described above) applied to their data resulted in similar measurements

as reported in their paper. We also include measurements of the two atomic carbon lines from four strong lenses in *Planck*’s dusty Gravitationally Enhanced sub-Millimetre Sources (GEMS; Nesvadba et al. 2019), as well as CO(7–6) and CO(4–3) line luminosity from Cañameras et al. (2018); all of these sources have lens models (Cañameras et al. 2015). For completeness, in our comparison of [CII](1–0) line luminosities we include field samples from Birkin et al. (2021), Alaghband-Zadeh et al. (2013), Huber et al. (in prep.), and Liao et al. (2024), although these samples do not have corresponding [CII](2–1) measurements. For the Gururajan et al. (2023) and Birkin et al. (2021) samples, we use S_{870} instead of S_{850} because S_{850} measurements were unavailable. Although we compare with the other samples above, only the Gururajan et al. (2023) and GEMS samples have both [CII](1–0) and [CII](2–1) measurements.

Walter et al. (2011) also observed the [CII](1–0) and [CII](2–1) lines in a sample of DSFGs and active galactic nuclei (AGN) at a median redshift of 2.8. They found a mean CII line ratio of 0.55 ± 0.15 (in L' units), comparable to the Gururajan et al. (2023) sample (see Fig. 2). However, we do not include this literature sample here to avoid confusing the results with the inclusion of AGN and because the median redshift of the sample is much lower than our sample.

The GEMS sample appears to have a lower $L_{\text{[CII]}(2-1)} / L_{\text{[CII]}(1-0)}$ ratio than the Gururajan et al. (2023) sample. Therefore, we only include the Gururajan et al. (2023) sample in the fits and statistics calculations we describe below to have a consistent comparison across all plots and to avoid exaggerating the difference in the $L_{\text{[CII]}(2-1)} / L_{\text{[CII]}(1-0)}$ ratio between the SPT2349–56 and field samples.

Next, we compute the means and standard deviations of the line ratios of the two samples, focusing on L' units which are more widely used in the literature; the results are shown in Fig. 2. We include the Gururajan et al. (2023) sources without lens models in this calculation, under the assumption that both lines are magnified equally. We draw 10^5 realizations of [CII](1–0) and [CII](2–1) line measurements from Gaussian distributions using the line measurement errors, giving 10^5 realizations of $L'_{\text{[CII]}(2-1)} / L'_{\text{[CII]}(1-0)}$ values for each source. Each realization has a mean and standard deviation for the protocluster and field sample from which we calculate an average and spread. We find a significantly higher mean atomic carbon line luminosity ratio in the SPT2349–56 sample ($\mu = 1.094 \pm 0.090$) compared to the field sample ($\mu = 0.671 \pm 0.052$), with standard deviations of $\sigma = 0.42 \pm 0.11$ and $\sigma = 0.268 \pm 0.092$ for the protocluster sample and the field galaxy sample, respec-

tively. Additionally, we find a significantly higher median line luminosity ratio in the SPT2349–56 sample (median = 0.94, interquartile range = 0.81–1.24) compared to the field sample (median = 0.55, interquartile range = 0.50–0.76).

For completeness, for the $L'_{\text{CO}(7-6)} / L'_{\text{CO}(4-3)}$ ratios we find a mean of $\mu = 0.604 \pm 0.029$ for the protocluster sample and $\mu = 0.466 \pm 0.033$ for the field sample (with $\sigma = 0.235 \pm 0.037$ and $\sigma = 0.281 \pm 0.088$, respectively). The $L'_{\text{CO}(7-6)} / L'_{\text{CO}(4-3)}$ medians are 0.55 and 0.39, with interquartile ranges of 0.48–0.68 and 0.33–0.47. These results suggest a potential difference in physical properties such as the gas kinetic temperature and density, however a more detailed analysis modeling the full suite of available CO data will be carried out in a future work (Sulzenauer et al. in prep.).

Turning to the [C I](1–0) and [C I](2–1) line luminosity versus S_{850} (Fig. 2), we fit power laws of the form $L = \alpha_{\text{C}} (S_{850}/S_{\text{x}})^{\gamma}$ to the protocluster and field samples separately, where C_{y} is fixed to $3 \times 10^7 L_{\odot}$ and S_{x} to 7 mJy so that our fit parameters are unitless and of order unity. The fits were done with an orthogonal distance regression using `scipy`’s `odr` module. In Fig. 2 the fits to the field sample are shown in red and the fits to the SPT2349–56 galaxies are shown in blue, each with the 95% confidence region shaded in. The values and 1σ uncertainties in the fit parameters are also shown in the figure. We find similar fit parameters to the [C I](1–0) line luminosities in both populations, while the amplitude of the [C I](2–1) fit is significantly larger for the protocluster sample versus the field sample.

To compare the power law fits, we calculated the average [C I] line luminosity ratios (defined as $r = L_{\text{C}} / L_{\text{F}}$, where ‘C’ denotes cluster and ‘F’ denotes field) predicted by the fits over the interval between 2 and 20 mJy, where most of the data is situated. As the data is uniformly distributed logarithmically with respect to S_{850} , we calculated \bar{r} with respect to $\log\left(\frac{S_{850}}{S_{\text{x}}}\right)$ as:

$$\bar{r} = \frac{\alpha_{\text{C}}}{\alpha_{\text{F}} \log\left(\frac{20}{2}\right)} \int_{\log\left(\frac{2 \text{ mJy}}{S_{\text{x}}}\right)}^{\log\left(\frac{20 \text{ mJy}}{S_{\text{x}}}\right)} 10^{(\gamma_{\text{C}} - \gamma_{\text{F}})u} du \quad (1)$$

where $u = \log\left(\frac{S_{850}}{S_{\text{x}}}\right)$. We find $\bar{r}_{10} = 1.41 \pm 0.26$ for [C I](1–0) and $\bar{r}_{21} = 2.17 \pm 0.38$ for [C I](2–1), suggesting an excess of [C I](2–1) / S_{850} in SPT2349–56 compared to the field. Additionally, we find $\frac{\bar{r}_{21}}{\bar{r}_{10}} = 1.54 \pm 0.39$ which is consistent with the ratio of the mean $L_{[\text{C I}](2-1)} / L_{[\text{C I}](1-0)}$ values between the field and SPT2349–56, 1.63 ± 0.18 .

Being a simple three-level quantum system and assuming local thermal equilibrium, the [C I](1–0) and [C I](2–1) line luminosities can be used to calculate the gas ex-

citation temperature, T_{ex} , as (Schneider et al. 2003):

$$T_{\text{ex}} = \frac{38.8 \text{ K}}{\ln\left(\frac{2.11}{R_{\text{CI}}}\right)}, \quad (2)$$

with R_{CI} in the above equation given by

$$R_{\text{CI}} = \frac{L'_{[\text{C I}](2-1)}}{L'_{[\text{C I}](1-0)}}. \quad (3)$$

We note that these equations assume that both C I lines are optically thin and that the emission arises from photon-dominated regions (PDRs). We find optical depths of $< 5 \times 10^{-3}$ for both C I lines across our sample, sufficiently thin to apply Eq. 2. In principle the C I gas might not be in thermal equilibrium, and so knowledge of the gas density would be required to estimate the gas temperature more precisely (Papadopoulos et al. 2022); however, we regardless expect a positive correlation between the line ratios and gas temperatures for our samples of protocluster and field DSFGs.

Using the mean R_{CI} for SPT2349–56, we find $T_{\text{ex}} = 59.1^{+8.1}_{-6.8}$ K. On the other hand, using the mean R_{CI} from the Gururajan et al. (2023) sample, we find $T_{\text{ex}} = 33.9^{+2.4}_{-2.2}$ K; here the errorbars are 68% confidence intervals, propagated from the (Gaussian) uncertainties in the mean line luminosity ratios. It is worth pointing out that one of the galaxies in SPT2349–56 (C6) has been detected in several radio bands, making it a likely AGN (Chapman et al. 2024). Neutral carbon line emission from AGN tend to come from X-ray-dominated regions (XDRs) as opposed to PDRs, the latter of which is assumed in deriving Eq. 2. However, the line luminosity ratio for C6 is by no means an outlier in our sample, and removing it from our sample has no effect on our sample statistics, so we proceed with the results above. Neutral carbon line luminosity ratios $L'_{[\text{C I}](2-1)} / L'_{[\text{C I}](1-0)} \gtrsim 0.8$ have been suggested to be an indication of AGN due to X-ray heating (e.g. Meijerink et al. 2007), although further observational evidence would be required to confirm additional AGN in the SPT2349–56 protocluster.

Lastly, it is worth pointing out that additional trends in the $L'_{[\text{C I}](2-1)} / L'_{[\text{C I}](1-0)}$ ratio might be present. Physical protocluster galaxy size estimates from 870 μm dust continuum and [C II] line emission observations are available from Hill et al. (2020) and Hill et al. (2022), respectively, however no correlations were seen. We also looked for correlations between the line strength ratio and distance from the protocluster center, but again we did not find any trends.

4. DISCUSSION AND CONCLUSIONS

Our main finding is an excess in the [C I](2–1) line luminosities in the protocluster galaxies found in

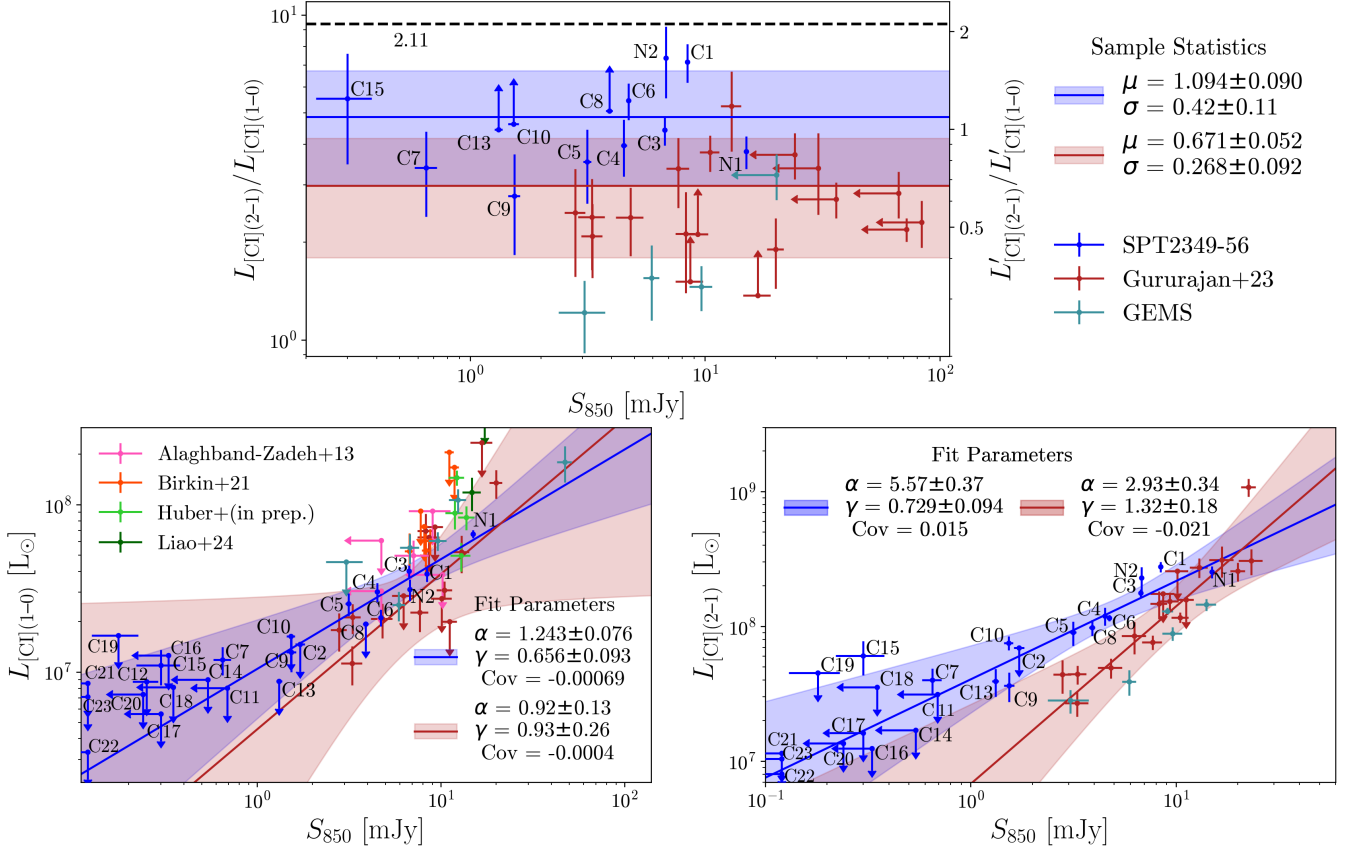


Figure 2. Comparison of [CII] and CO line luminosities and line ratios in SPT2349–56 and the literature field sample. *Top:* The $L_{[\text{CII}](2-1)} / L_{[\text{CII}](1-0)}$ ratio as a function of S_{850} for protocluster galaxies (blue) and field galaxies (red), with L' units shown on the right axis. The horizontal dashed line at $L'_{[\text{CII}](2-1)} / L'_{[\text{CII}](1-0)} = 2.11$ indicates where the line ratio becomes unphysical (see Eq. 2). Sources with $> 3.5\sigma$ measurements in both lines are shown as detections, otherwise we show upper/lower limits. The mean and scatter of the samples are shown as the solid lines and shaded regions, respectively. *Bottom left:* $L_{[\text{CII}](1-0)}$ versus S_{850} for protocluster galaxies versus field galaxies. Upper limits are shown for measurements below 3.5σ . Best-fit power law models to both SPT2349–56 (blue) and Gururajan et al. (2023) (red) samples are shown as the solid lines, with the fit parameters and covariances listed. The shaded regions correspond to 95% confidence intervals assuming the fit parameters α and γ follow a multivariate normal distribution. *Bottom right:* Same as bottom left but for $L_{[\text{CII}](2-1)}$.

SPT2349–56 compared to field DSFGs at similar redshifts (for a given $850\ \mu\text{m}$ flux density), while the [CII](1–0) line luminosities are comparable. The difference means that protocluster galaxies have a higher gas excitation temperature ($T_{\text{ex}} = 59.1^{+8.1}_{-6.8}$ K) compared to field galaxies ($T_{\text{ex}} = 33.9^{+2.4}_{-2.2}$ K).

A key aspect is that our findings are not very sensitive to the actual L_{FIR} values of the galaxies in either sample. If the dust temperatures of the protocluster galaxies in SPT2349–56 are higher than the field galaxies in our comparison sample, then we would interpret the higher line ratios as a deficit in [CII](1–0) (as opposed to an excess in [CII](2–1)), but our results based on the line ratios would not change. In addition, we note that Hill et al. (2022) found evidence that the gas depletion timescales (effectively the ratio of CO(4–3) line luminosity to L_{FIR}) of the protocluster galaxies in

SPT2349–56 are smaller than for field galaxies, consistent with them having higher radiation intensity per unit gas mass, and therefore higher excitation temperatures. Our result is also robust against potential beam effects as the smaller Band 4 beam would tend to over-resolve flux compared to the larger Band 3 beam leading to a smaller line ratio, and we have tested several line strength measurement techniques. We have also tested for the potential of spectral confusion between [CII](2–1) and CO(7–6) by running our algorithm directly on the comparison field sample.

(Cortzen et al. 2020) also measured the [CII](1–0) and [CII](2–1) transitions in GN20, a well-studied DSFG ($S_{850} \approx 20$ mJy, Pope et al. 2006) at $z = 4.05$. This galaxy is potentially the central site of a protocluster (Daddi et al. 2009), although the number of spectroscopically-confirmed DSFGs is four, much less

than the number of DSFGs found in SPT2349–56, and the luminosity distribution is heavily weighted towards the extremely luminous GN20. Nonetheless, (Cortzen et al. 2020) found a high $L'_{\text{[CII]}(2-1)}/L'_{\text{[CII]}(1-0)}$ ratio of 0.94 ± 0.18 , corresponding to a [CII] gas excitation temperature of 48^{+14}_{-9} K and comparable to the mean value found in SPT2349–56.

Several interpretations are possible. Simulations show that close-by interactions can drive gas towards the centers of galaxies, thereby increasing the observed average density and gas excitation temperature (e.g., Moreno et al. 2015; Blumenthal & Barnes 2018; Moreno et al. 2019). Alternatively, the protocluster galaxies in SPT2349–56 could have had their less dense outer regions (traced by $L_{\text{[CII]}(1-0)}$) stripped during these interactions, leaving an excess abundance of more centrally-concentrated gas (traced by $L_{\text{[CII]}(2-1)}$).

It is worth noting that Hill et al. (2022) compared the gas mass-to-stellar mass ratios (with gas mass scaled from CO(4–3) detections) of the protocluster galaxies in SPT2349–56 to field galaxies found around the same redshift, finding no significant difference between the two populations. Thus to explain our observations with the gas stripping scenario, cold gas (with normal $L_{\text{[CII]}(2-1)}/L_{\text{[CII]}(1-0)}$ ratios, similar to field galaxies) must be feeding the core of SPT2349–56 to provide an initial excess in gas mass, which is subsequently lost to the forming intergalactic medium. While both the gas stripping and the centrally-concentrated gas scenarios are possible, the latter is simpler and therefore our preferred explanation.

Atomic carbon line luminosities have also been proposed as a gas mass tracer (comparable to CO; e.g., Papadopoulos et al. 2004; Papadopoulos & Greve 2004; Bothwell et al. 2017; Dunne et al. 2021), and so it is worth investigating how robust previous gas mass estimates are. The molecular gas mass (M_{H_2}) can be written as (Gururajan et al. 2023)

$$M_{\text{H}_2} = \frac{k L_{\text{[CII]}(1-0)}}{Q_{10} X_{\text{CI}}} [\text{M}_{\odot}], \quad (4)$$

where

$$Q_{10} = \frac{3 \exp(-\frac{T_1}{T_{\text{ex}}})}{1 + 3 \exp(-\frac{T_1}{T_{\text{ex}}}) + 5 \exp(-\frac{T_2}{T_{\text{ex}}})}, \quad (5)$$

$k = 3.39 \times 10^{-2} \text{ M}_{\odot} \text{ L}_{\odot}^{-1}$, $T_1 = 23.6 \text{ K}$, $T_2 = 62.5 \text{ K}$, and X_{CI} is the calibration factor (equal to the neutral [CI]/[H₂] abundance ratio). Gururajan et al. (2023) combined their sample with other literature DSFGs to derive a mean calibration factor of $X_{\text{CI}} \times \alpha_{\text{CO}} = (6.31 \pm 0.67) \times 10^{-5}$, which we apply to our sample along with

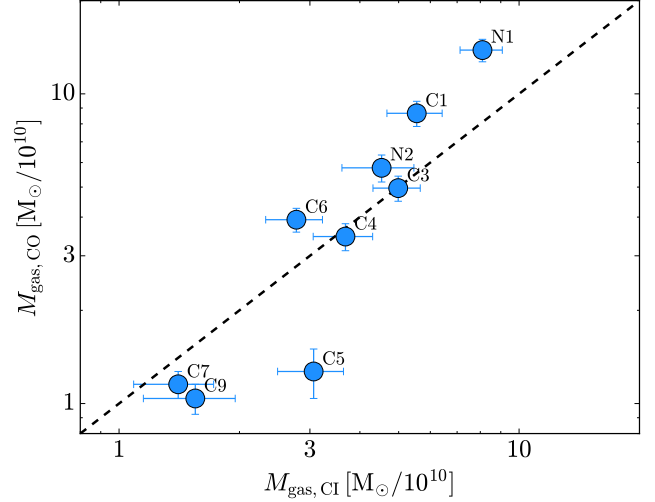


Figure 3. Gas mass estimates from CO(4–3) measurements compared to gas mass estimates from [CI]. Hill et al. (2020) assumed $r_{4,1} = 0.60 \pm 0.05$ to convert CO(4–3) to CO(1–0) line luminosities (in units of $\text{K km s}^{-1} \text{ pc}^2$) and $\alpha_{\text{CO}} = 1.0 \text{ M}_{\odot} (\text{K km s}^{-1} \text{ pc}^2)^{-1}$. We have used Eq. 4 with $X_{\text{CI}} \times \alpha_{\text{CO}} = (6.31 \pm 0.67) \times 10^{-5}$ (Gururajan et al. 2023), along with the same α_{CO} value.

$\alpha_{\text{CO}} = 1.0 \text{ M}_{\odot} (\text{K km s}^{-1} \text{ pc}^2)^{-1}$ (as was used by Hill et al. 2020). In Fig. 3 we compare the gas masses from Hill et al. (2020) (derived from CO(4–3), assuming $r_{4,1} = 0.60 \pm 0.05$) to gas masses derived from [CI] (using Eq. 4). We find good agreement between the overall calibration factors applied to the two mass estimates, with a small systematic error leading to a slight tilt in the $M_{\text{gas, CI}} - M_{\text{gas, CO}}$ relation. However, this tilt only leads to differences between the two gas mass tracers within a factor of 2.

The two main interpretations we have discussed regarding the difference in [CI] line luminosity ratios between protocluster galaxies and field galaxies at high redshift, namely nearby interactions either driving cold gas to the cores of the protocluster galaxies or stripping gas from the less dense outskirts, cannot be conclusively distinguished with our current data. Further ALMA observations directly measuring the far-infrared continuum (thus constraining the overall dust continuum temperatures), along with bolstering the result with lower $J = 1-0$ and $2-1$ CO measurements of the cold gas, will allow a more complete explanation of the results. Measuring additional molecular and fine structure lines and performing detailed PDR modelling will further elucidate any differences in the ISM conditions.

Ultimately, SPT2349–56 provides a key laboratory for probing how efficiently star formation is maintained during the collapse of a protocluster, with potentially important implications for the build-up of the intraculus

ter medium, the early enrichment of the intracluster medium with metals, and the quenching of cluster galaxies at high redshift.

ACKNOWLEDGMENTS

We would like to thank Desika Narayanan for helpful comments and input. This paper makes use of the following ALMA data: ADS/JAO.ALMA#2017.1.00273.S, #2018.1.00018.S, and #2021.1.01313.S. ALMA is a partnership of ESO (representing its member states), NSF (USA) and NINS (Japan), together with NRC (Canada), MOST and ASIAA (Taiwan), and KASI (Republic of Korea), in cooperation with the Republic of Chile. The Joint ALMA Observatory is operated by ESO, AUI/NRAO and NAOJ. The National Radio Astronomy Observatory is a facility of the National Science Foundation operated under cooperative agreement by Associated Universities, Inc. S.C. and R.H. gratefully acknowledge support for this research from NSERC. MA acknowledges support from ANID Basal Project FB210003 and ANID MILENIO NCN2024_112. The Cosmic Dawn Center (DAWN) is funded by the Danish National Research Foundation under grant No. 140.

REFERENCES

- Alaghband-Zadeh, S., Chapman, S. C., Swinbank, A. M., et al. 2013, *MNRAS*, 435, 1493, doi: [10.1093/mnras/stt1390](https://doi.org/10.1093/mnras/stt1390)
- Andreon, S. 2003, *A&A*, 409, 37, doi: [10.1051/0004-6361:20031073](https://doi.org/10.1051/0004-6361:20031073)
- Andrews, M., Artale, M. C., Kumar, A., et al. 2024, arXiv e-prints, arXiv:2410.08412, doi: [10.48550/arXiv.2410.08412](https://doi.org/10.48550/arXiv.2410.08412)
- Apostolovski, Y., Aravena, M., Anguita, T., et al. 2024, *A&A*, 683, A64, doi: [10.1051/0004-6361/202245785](https://doi.org/10.1051/0004-6361/202245785)
- Bayet, E., Gerin, M., Phillips, T. G., & Contursi, A. 2009, *MNRAS*, 399, 264, doi: [10.1111/j.1365-2966.2009.15258.x](https://doi.org/10.1111/j.1365-2966.2009.15258.x)
- Birkin, J. E., Weiss, A., Wardlow, J. L., et al. 2021, *MNRAS*, 501, 3926, doi: [10.1093/mnras/staa3862](https://doi.org/10.1093/mnras/staa3862)
- Blumenthal, K. A., & Barnes, J. E. 2018, *MNRAS*, 479, 3952, doi: [10.1093/mnras/sty1605](https://doi.org/10.1093/mnras/sty1605)
- Bothwell, M. S., Aguirre, J. E., Aravena, M., et al. 2017, *MNRAS*, 466, 2825, doi: [10.1093/mnras/stw3270](https://doi.org/10.1093/mnras/stw3270)
- Cañameras, R., Nesvadba, N. P. H., Guery, D., et al. 2015, *A&A*, 581, A105, doi: [10.1051/0004-6361/201425128](https://doi.org/10.1051/0004-6361/201425128)
- Cañameras, R., Yang, C., Nesvadba, N. P. H., et al. 2018, *A&A*, 620, A61, doi: [10.1051/0004-6361/201833625](https://doi.org/10.1051/0004-6361/201833625)
- Chapman, S. C., Hill, R., Aravena, M., et al. 2024, *ApJ*, 961, 120, doi: [10.3847/1538-4357/ad0b77](https://doi.org/10.3847/1538-4357/ad0b77)
- Chiang, Y.-K., Overzier, R. A., Gebhardt, K., & Henriques, B. 2017, *ApJL*, 844, L23, doi: [10.3847/2041-8213/aa7e7b](https://doi.org/10.3847/2041-8213/aa7e7b)
- Cortzen, I., Magdis, G. E., Valentino, F., et al. 2020, *A&A*, 634, L14, doi: [10.1051/0004-6361/201937217](https://doi.org/10.1051/0004-6361/201937217)
- Cramer, W. J., Noble, A. G., Rudnick, G., et al. 2024, *ApJ*, 975, 144, doi: [10.3847/1538-4357/ad7798](https://doi.org/10.3847/1538-4357/ad7798)
- Daddi, E., Dannerbauer, H., Stern, D., et al. 2009, *ApJ*, 694, 1517, doi: [10.1088/0004-637X/694/2/1517](https://doi.org/10.1088/0004-637X/694/2/1517)
- Dunne, L., Maddox, S. J., Vlahakis, C., & Gomez, H. L. 2021, *MNRAS*, 501, 2573, doi: [10.1093/mnras/staa3526](https://doi.org/10.1093/mnras/staa3526)
- Ellis, R. S., Smail, I., Dressler, A., et al. 1997, *ApJ*, 483, 582, doi: [10.1086/304261](https://doi.org/10.1086/304261)
- Everett, W. B., Zhang, L., Crawford, T. M., et al. 2020, *ApJ*, 900, 55, doi: [10.3847/1538-4357/ab9df7](https://doi.org/10.3847/1538-4357/ab9df7)
- Gururajan, G., Bethermin, M., Sulzenauer, N., et al. 2023, *A&A*, 676, A89, doi: [10.1051/0004-6361/202346449](https://doi.org/10.1051/0004-6361/202346449)
- Hill, R., Chapman, S., Scott, D., et al. 2020, *MNRAS*, 495, 3124, doi: [10.1093/mnras/staa1275](https://doi.org/10.1093/mnras/staa1275)
- Hill, R., Chapman, S., Phadke, K. A., et al. 2022, *MNRAS*, 512, 4352, doi: [10.1093/mnras/stab3539](https://doi.org/10.1093/mnras/stab3539)
- Hine, N. K., Geach, J. E., Alexander, D. M., et al. 2016, *MNRAS*, 455, 2363, doi: [10.1093/mnras/stv2448](https://doi.org/10.1093/mnras/stv2448)
- Ivison, R. J., Biggs, A. D., Bremer, M., Arumugam, V., & Dunne, L. 2020, *MNRAS*, 496, 4358, doi: [10.1093/mnras/staa1802](https://doi.org/10.1093/mnras/staa1802)
- Lee-Brown, D. B., Rudnick, G. H., Momcheva, I. G., et al. 2017, *ApJ*, 844, 43, doi: [10.3847/1538-4357/aa7948](https://doi.org/10.3847/1538-4357/aa7948)
- Liao, C.-L., Chen, C.-C., Wang, W.-H., et al. 2024, *The Astrophysical Journal*, 961, 226, doi: [10.3847/1538-4357/ad148c](https://doi.org/10.3847/1538-4357/ad148c)

- Liu, D., Gao, Y., Isaak, K., et al. 2015, *ApJL*, 810, L14, doi: [10.1088/2041-8205/810/2/L14](https://doi.org/10.1088/2041-8205/810/2/L14)
- Lotz, J. M., Papovich, C., Faber, S. M., et al. 2013, *ApJ*, 773, 154, doi: [10.1088/0004-637X/773/2/154](https://doi.org/10.1088/0004-637X/773/2/154)
- McMullin, J. P., Waters, B., Schiebel, D., Young, W., & Golap, K. 2007, in *Astronomical Society of the Pacific Conference Series*, Vol. 376, *Astronomical Data Analysis Software and Systems XVI*, ed. R. A. Shaw, F. Hill, & D. J. Bell, 127
- Meijerink, R., Spaans, M., & Israel, F. P. 2007, *A&A*, 461, 793, doi: [10.1051/0004-6361/20066130](https://doi.org/10.1051/0004-6361/20066130)
- Miller, T. B., Chapman, S. C., Aravena, M., et al. 2018, *Nature*, 556, 469, doi: [10.1038/s41586-018-0025-2](https://doi.org/10.1038/s41586-018-0025-2)
- Moreno, J., Torrey, P., Ellison, S. L., et al. 2015, *MNRAS*, 448, 1107, doi: [10.1093/mnras/stv094](https://doi.org/10.1093/mnras/stv094)
- . 2019, *MNRAS*, 485, 1320, doi: [10.1093/mnras/stz417](https://doi.org/10.1093/mnras/stz417)
- Muzzin, A., Wilson, G., Yee, H. K. C., et al. 2012, *ApJ*, 746, 188, doi: [10.1088/0004-637X/746/2/188](https://doi.org/10.1088/0004-637X/746/2/188)
- Namiki, S. V., Koyama, Y., Hayashi, M., et al. 2019, *ApJ*, 877, 118, doi: [10.3847/1538-4357/ab1b6c](https://doi.org/10.3847/1538-4357/ab1b6c)
- Nesvadba, N. P. H., Cañameras, R., Kneissl, R., et al. 2019, *A&A*, 624, A23, doi: [10.1051/0004-6361/201833777](https://doi.org/10.1051/0004-6361/201833777)
- Oteo, I., Ivison, R. J., Dunne, L., et al. 2018, *ApJ*, 856, 72, doi: [10.3847/1538-4357/aaa1f1](https://doi.org/10.3847/1538-4357/aaa1f1)
- Overzier, R. A. 2016, *A&A Rv*, 24, 14, doi: [10.1007/s00159-016-0100-3](https://doi.org/10.1007/s00159-016-0100-3)
- Papadopoulos, P., Dunne, L., & Maddox, S. 2022, *MNRAS*, 510, 725, doi: [10.1093/mnras/stab3194](https://doi.org/10.1093/mnras/stab3194)
- Papadopoulos, P. P., & Greve, T. R. 2004, *ApJL*, 615, L29, doi: [10.1086/426059](https://doi.org/10.1086/426059)
- Papadopoulos, P. P., Thi, W. F., & Viti, S. 2004, *MNRAS*, 351, 147, doi: [10.1111/j.1365-2966.2004.07762.x](https://doi.org/10.1111/j.1365-2966.2004.07762.x)
- Pérez-Martínez, J. M., Kodama, T., Koyama, Y., et al. 2024, *MNRAS*, 527, 10221, doi: [10.1093/mnras/stad3805](https://doi.org/10.1093/mnras/stad3805)
- Planck Collaboration VI. 2020, *A&A*, 641, A6, doi: [10.1051/0004-6361/201833910](https://doi.org/10.1051/0004-6361/201833910)
- Pope, A., Scott, D., Dickinson, M., et al. 2006, *MNRAS*, 370, 1185, doi: [10.1111/j.1365-2966.2006.10575.x](https://doi.org/10.1111/j.1365-2966.2006.10575.x)
- Popescu, R., Pope, A., Lee, K.-S., et al. 2023, *ApJ*, 958, 12, doi: [10.3847/1538-4357/acee79](https://doi.org/10.3847/1538-4357/acee79)
- Rettura, A., Rosati, P., Nonino, M., et al. 2010, *ApJ*, 709, 512, doi: [10.1088/0004-637X/709/1/512](https://doi.org/10.1088/0004-637X/709/1/512)
- Reuter, C., Vieira, J. D., Spilker, J. S., et al. 2020, *ApJ*, 902, 78, doi: [10.3847/1538-4357/abb599](https://doi.org/10.3847/1538-4357/abb599)
- Rotermund, K. M., Chapman, S. C., Phadke, K. A., et al. 2021, *MNRAS*, 502, 1797, doi: [10.1093/mnras/stab103](https://doi.org/10.1093/mnras/stab103)
- Schneider, N., Simon, R., Kramer, C., et al. 2003, *A&A*, 406, 915, doi: [10.1051/0004-6361:20030726](https://doi.org/10.1051/0004-6361:20030726)
- Scoville, N., Arnouts, S., Aussel, H., et al. 2013, *ApJS*, 206, 3, doi: [10.1088/0067-0049/206/1/3](https://doi.org/10.1088/0067-0049/206/1/3)
- Spilker, J. S., Marrone, D. P., Aravena, M., et al. 2016, *ApJ*, 826, 112, doi: [10.3847/0004-637X/826/2/112](https://doi.org/10.3847/0004-637X/826/2/112)
- Steidel, C. C., Adelberger, K. L., Shapley, A. E., et al. 2005, *ApJ*, 626, 44, doi: [10.1086/429989](https://doi.org/10.1086/429989)
- Valentino, F., Daddi, E., Strazzullo, V., et al. 2015, *ApJ*, 801, 132, doi: [10.1088/0004-637X/801/2/132](https://doi.org/10.1088/0004-637X/801/2/132)
- Vulcani, B., Poggianti, B. M., Gullieuszik, M., et al. 2018, *ApJL*, 866, L25, doi: [10.3847/2041-8213/aae68b](https://doi.org/10.3847/2041-8213/aae68b)
- Walter, F., Weiß, A., Downes, D., Decarli, R., & Henkel, C. 2011, *ApJ*, 730, 18, doi: [10.1088/0004-637X/730/1/18](https://doi.org/10.1088/0004-637X/730/1/18)
- Webb, K., Balogh, M. L., Leja, J., et al. 2020, *MNRAS*, 498, 5317, doi: [10.1093/mnras/staa2752](https://doi.org/10.1093/mnras/staa2752)
- Weiß, A., Henkel, C., Downes, D., & Walter, F. 2003, *A&A*, 409, L41, doi: [10.1051/0004-6361:20031337](https://doi.org/10.1051/0004-6361:20031337)
- Zhou, D., Chapman, S. C., Sulzenauer, N., et al. 2025, *ApJL*, 982, L17, doi: [10.3847/2041-8213/adb8d8](https://doi.org/10.3847/2041-8213/adb8d8)

Table 2. Population statistics of the protocluster galaxies in SPT2349–56, including and excluding N1.

Including N1	Line	Power Law				CI Ratio		
		α	γ	Covariance	\bar{r}	μ	σ	T_{ex}
Yes	[C _I](1–0)	1.243±0.076	0.656±0.093	-0.00069	1.41±0.26	1.094±0.090	0.42±0.11	59.1 ^{+8.1} _{-6.8} K
	[C _I](2–1)	5.57±0.37	0.729±0.094	0.015	2.17±0.38			
No	[C _I](1–0)	1.122±0.089	0.48±0.10	0.0047	1.34±0.26	1.120±0.099	0.43±0.12	61.3 ^{+8.4} _{-7.1} K
	[C _I](2–1)	5.96±0.48	0.84±0.13	0.041	2.24±0.38			

APPENDIX

A. IMPACT OF N1 ON THE PROTOCLUSTER SAMPLE STATISTICS

N1 is the brightest source in SPT2349–56 and thus has the most weight when calculating the population statistics, yet this source is certainly not representative of the typical protocluster galaxy. The power law fit parameters and [C_I] ratio sample statistics calculated excluding N1 are therefore shown in Table 2 for comparison. Using the mean R_{CI} for SPT2349–56 calculated without N1, we find $T_{\text{ex}} = 61.3^{+8.4}_{-7.1}$ K. Excluding N1 therefore does not have a large effect on the population statistics we have calculated.

B. SPATIALLY-COINCIDENT [C_I] AND [C_{II}] LINE EMISSION CUTOUTS

Here we provide [C_I](1–0), [C_I](2–1), and [C_{II}] cutouts of the protocluster galaxies in SPT2349–56 after averaging over the integration range used in our line detection pipeline. Fig. 4 shows [C_{II}] cutouts and contours (blue) in steps of $2^n\sigma$, where $n = 0, 1, 2, 3, \dots$, with [C_I](1–0) (red) and [C_I](2–1) (yellow) contours overlaid at the same σ levels for comparison. For all lines, the integration range was set to 2σ around the center of the line. The peak pixel in the [C_{II}] cutouts are indicated by circles, and we find that for most of our $> 2.5\sigma$ detections, the [C_{II}] falls within the 2σ contours of the [C_I](1–0) and [C_I](2–1) maps.

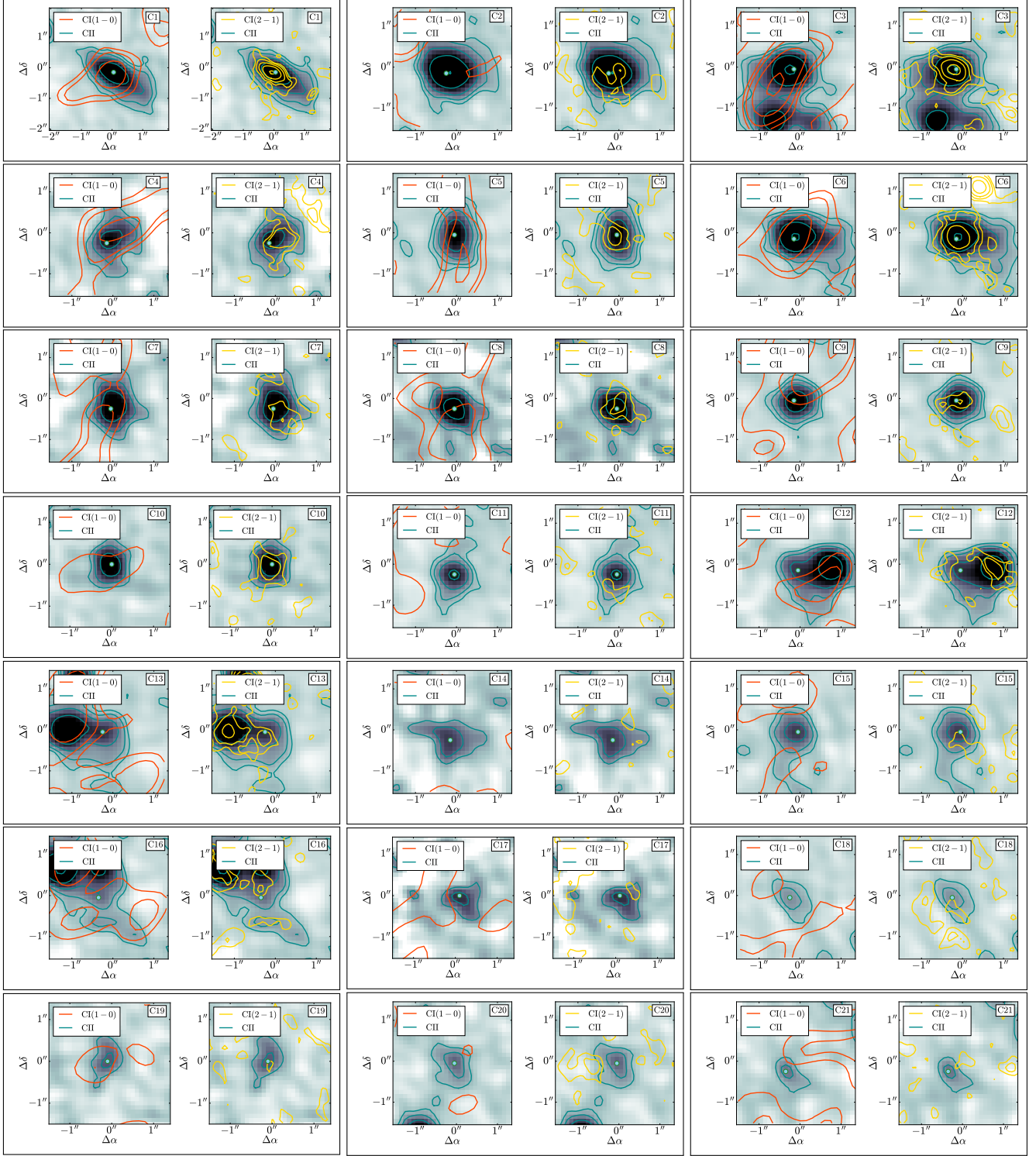
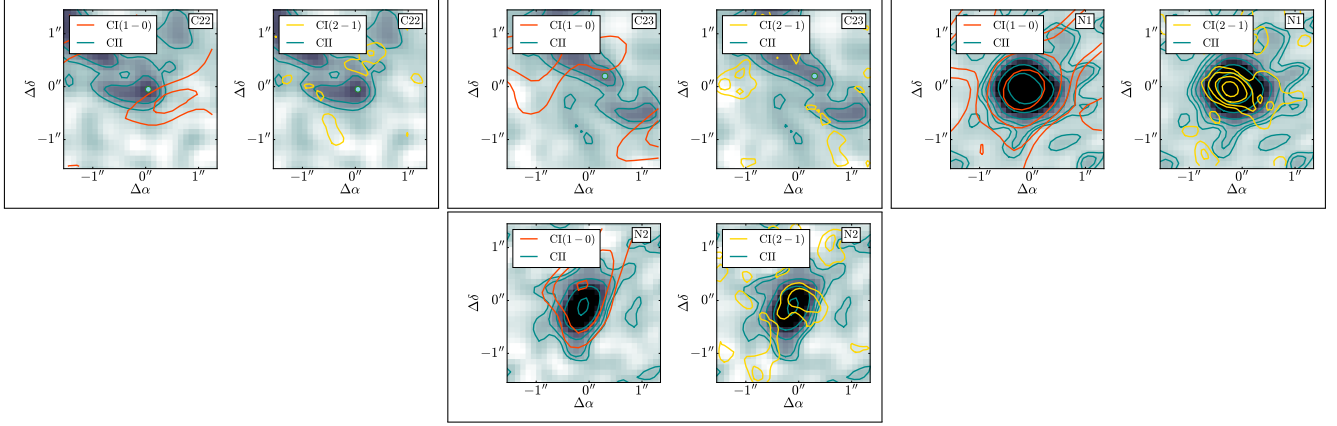


Figure 4. [CII] cutouts from [Hill et al. \(2020\)](#) are shown in the background, with blue contours overlaid in steps of $2^n\sigma$ (where $n=0, 1, 2, 3, \dots$). [CI](1-0) (red) and [CI](2-1) (yellow) contours are overlaid following the same σ levels for comparison. The peak pixel in the [CII] cutouts are indicated by circles. In all cases the line integration ranges are 2σ around the centers of the lines. The [CI](2-1) maps have been lightly smoothed by a Gaussian with a standard deviation of 1 pixel for presentation purposes.

**Figure 4.** Continued.